Mineralogical Magazine, August 2013, Vol. 77(6), pp. 2867–2882

Alpha particle damage in biotite characterized by microfocus X-ray diffraction and Fe *K*-edge X-ray absorption spectroscopy

R. A. D. Pattrick[1,*], J. M. Charnock[1], T. Geraki[2], J. F. W. Mosselmans[2], C. I. Pearce[3], S. Pimblott[3] and G. T. R. Droop[1]

[1] School of Earth, Atmospheric and Environmental Sciences and the Williamson Research Centre, The University of Manchester, Manchester M13 9PL, UK
[2] Diamond Light Source, Rutherford Appleton Laboratories, Didcott, Oxfordshire OX11 0QX, UK
[3] School of Chemistry, The University of Manchester, Manchester M13 9PL, UK and Dalton Cumbrian Facility, The University of Manchester, Westlakes Science and Technology Park, Cumbria CA24 3HA, UK

[*Received 26 December 2012; Accepted 4 July 2013; Associate Editor: F. Cámara*]

ABSTRACT

Combined microfocus XAS and XRD analysis of α-particle radiation damage haloes around thorium-containing monazite in Fe-rich biotite reveals changes in both short- and long-range order. The total α-particles flux derived from the Th and U in the monazite over 1.8 Ga was 0.022 α particles per atomic component of the monazite and this caused increasing amounts of structural damage as the monazite emitter is approached. Short-range order disruption revealed by Fe *K*-edge EXAFS is manifest by a high variability in Fe–Fe bond lengths and a marked decrease in coordination number. XANES examination of the Fe *K*-edge shows a decrease in energy of the main absorption by up to 1 eV, revealing reduction of the Fe^{3+} components of the biotite by interaction with the ${}^{4}_{2}He^{2+}$, the result of low and thermal energy electrons produced by the cascade of electron collisions. Changes in *d* spacings in the XRD patterns reveal the development of polycrystallinity and new domains of damaged biotite structure with evidence of displaced atoms due to ionization interactions and nuclear collisions. The damage in biotite is considered to have been facilitated by destruction of OH groups by radiolysis and the development of Frenkel pairs causing an increase in the trioctahedral layer distances and contraction within the trioctahedral layers. The large amount of radiation damage close to the monazite can be explained by examining the electronic stopping flux.

Keywords: α-particle damage, monazite, biotite, haloes.

Introduction

Radiation damage in biotite is a product of α-particle (${}^{4}_{2}He^{2+}$) bombardment derived from actinides (U/Th) substituted into the structure of minerals such as zircon ($ZrSiO_4$) and monazite ($CePO_4$). The classic occurrence (Joly, 1917; Gentry, 1974) is a sphere of damage around an actinide-bearing-inclusion, manifest as a brown halo in rock thin section, often spreading ~35 μm from the inclusion, with a relatively sharp outer edge (Fig. 1). The radiation damage in biotite ($K(Mg,Fe)_3(AlSi_3O_{10}(OH,F)_2)$) is different from the more extensively studied damage in the actinide-bearing minerals where the α-emitter is within the mineral structure. In these latter phases, the damage is due largely to recoil of the daughter nucleus after α-particle emission, which takes place on a nm scale and causes a loss of crystallinity with resulting metamictization and

* E-mail: richard.pattrick@manchester.ac.uk
DOI: 10.1180/minmag.2013.077.6.12

© 2013 The Mineralogical Society

https://doi.org/10.1180/minmag.2013.077.6.12 Published online by Cambridge University Press

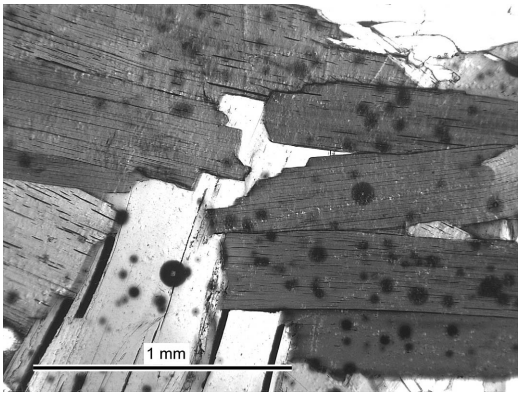

FIG. 1. Radiation damage haloes showing as dark circles surrounding monazite inclusions (lighter centres) in biotite (darker, cleaved phase) in a 1.8 Ga meta-ironstone from Tunaberg, Sweden (optical image in plane polarized light).

amorphization (Murakami *et al*., 1991; Weber *et al*., 1994; Ewing, 2001; Nasdala *et al*., 2005). In a study of radio-haloes in biotite, Nasdala *et al*. (2001) used modelling and Raman spectroscopy to examine the nature of the biotite surrounding U-bearing zircon inclusions. Their Monte Carlo simulations predict an α-particle penetration of the biotite of up to 37.3 μm with the optically visible halo a function of the point defect generation; the calculated highest density of these defects was 1/100 atoms, indicating the biotite lattice should be largely preserved. In the experimental component of their study, the broadening and intensity loss in the Raman spectra, suggested significant disruption to the short-range order in the biotite while the lack of changes in optical absorbance spectra, especially the Fe^{2+}/Fe^{3+} absorption bands, indicated ionization effects were not important and, thus, there were no detectable redox changes in the iron in the biotite. The Raman microprobe information revealed an increasing loss of intensity, broadening of bands and band shifts as the actinide emitter was approached, although this was not uniform. The loss of intensity of the OH-band is interpreted as relating to charge imbalances around the H atoms caused by displacive or ionizing events. High-resolution transmission electron microscopy (HRTEM), however, also indicated a low degree of major structural damage (Nasdala *et al*., 2001).

In this study we have examined the structural changes in biotites with optically visible damage haloes developed around monazite inclusions using the combined X-ray diffraction (XRD) and X-ray absorption spectroscopy (XAS) microfocus capability of beamline I18 at the Diamond Light Source, UK.

Biotite and monazite chemistry

The biotite chosen for study is from an almandine-grunerite-biotite rock from near Strömshult, Tunaberg, Södermanland District, Sweden which belongs to the Proterozoic Svecofennian domain of the Fenno-Scandian Shield (Zhao *et al*., 2002). The sample came from a meta-ironstone layer with the granulite-facies mineral assemblage almandine + fayalite + hedenbergite ± ferrosilite (Palmgren, 1917; Sundius, 1932; Henry, 1935). The biotite-rich rock is an amphibolite-facies variant that has undergone extensive potassium metasomatism although there is no evidence of thermal events in the region in the last 1.5 Ga. The rock is medium- to coarse-grained and consists of irregular equant garnet crystals set in a matrix of randomly oriented subhedral biotite flakes and grunerite prisms. The biotite flakes measure up to 6 mm across and have aspect ratios of ~5:1 (Fig. 1). The biotite is peppered with dark brown (almost opaque) 30–40 μm-wide haloes around tiny (<10 μm diameter) monazite inclusions (Fig. 1). Some of the haloes can be divided into an inner dark brown zone and an outer, less intensely coloured zone 10–15 μm wide.

Major-element analyses of the biotite and monazite were undertaken by WDS-spectrometry using the Cameca SX-100 electron-microprobe at the University of Manchester. Standards used for biotite were fayalite (for Fe), tephroite (Mn), wollastonite (Ca and Si), rutile (Ti), K-feldspar (K), Cr_2O_3 (Cr), corundum (Al), jadeite (Na) and periclase (Mg). For monazite, UAl (U), $ThSiO_3$ (Th), galena (Pb), doped glass (*REE*) and wollastonite (Ca and Si). Analyses were performed at an accelerating voltage of 15 keV and a beam current of 20 nA, data were processed using PAP software (Pouchou and Pichoir, 1991). Analyses were obtained on traverses extending from halo interiors to areas of apparently undamaged biotite outside the haloes. The mean composition of 'undamaged' biotites (n = 42 in four traverses in different crystals) is: $K_{0.94}Na_{0.03}Fe_{1.95}Mg_{0.91}Mn_{0.05}Ti_{0.02}Al_{1.25}Si_{2.84}O_{10}(OH)_2$ and of the halo biotites (n = 24 in four traverses) it is: $K_{0.94}Na_{0.03}Fe_{1.95}Mg_{0.92}Mn_{0.05}Ti_{0.02}Al_{1.24}$

https://doi.org/10.1180/minmag.2013.077.6.12 Published online by Cambridge University Press

$Si_{2.84}O_{10}(OH)_2$. These are virtually indistinguishable and any variations noted were almost within analytical error (2σ) and not reproducible with respect to the haloes. Compared to most other biotite analyses (e.g. as listed in Fleet, 2003), this Tunaberg biotite has small Ti and Al contents, so that its composition falls close to the annite–phlogopite binary join. With all iron calculated as Fe^{2+}, every biotite analysis shows a small apparent octahedral+tetrahedral cation excess beyond the theoretical maximum of 7.00 per 11(O) anhydrous formula unit, suggesting that a minimum of 4% of iron is Fe^{3+}. Mössbauer analysis of the biotite separate from the Tunaberg sample used in this study was undertaken using aluminized polyethylene terephthalate (PETP) with one layer of 0.5 mm clear PETP holding the sample, and a capping layer of 0.075 mm PETP sealed with an epoxy resin to contain the powder anaerobically. Transmission ^{57}Fe Mössbauer spectra were collected at room temperature (~22ºC) using a FAST ComTec 1024-multichannel analyser system (γ-ray source: Co^{57}, 25 mCi). The spectra were fitted using Lorentzian line shapes with *Recoil* software version 1.05. Isomer shift data were calibrated with reference to metallic Fe foil. This revealed that 10% of the iron is Fe^{3+}. Halo biotite analyses show slightly higher cation excesses on average than undamaged biotites (0.03 as opposed to 0.02).

The monazite analyses determined by electron probe micro-analysis (EPMA) were of variable quality and low totals, a function of small inclusion size. They did, however, provide a good indication of the monazite chemistry which provided a mean composition of $(Ce_{0.40}La_{0.22}Nd_{0.12}Pr_{0.04}Sm_{0.03}Th_{0.15}U_{0.02}Si_{0.02})PO_4$. The monazites were high in La and Nd, low in the xenotine (Y) component and contained significant α-emitters at 2.5±0.3 at.% Th with 0.3±0.1 at.% U. The ^{232}Th and ^{238}U will produce 0.014 and 0.008 α-particles per atomic component, respectively, over the 1.8 Ga (see Table 1).

Radiation damage

The monazite of this study contains 2.5 at.% Th which will have been the main α-particle emitter. A small component can be accounted for as ^{234}Th

TABLE 1. α-emitting decay in the ^{232}Th and ^{238}U series show α -particle energies and calculated penetration depths through biotite. Energies and half-lives from NNDC, 2013. (Energies given as ground state to ground state, and depths recalculated from the Monte Carlo simulations of Nasdala *et al*., 2001.) The ^{232}Th decay series will dominate α particle bombardment and ^{238}U-series a much lesser contribution while spontaneous fission and ^{235}U-series will provide very minor contributions.

	Energy (MeV)	Depth in biotite (μm)	Half life
^{232}Th α-decay series			
$^{232}Th \rightarrow ^{228}Ra$	4.08	12.5	$1.405 \cdot 10^{10}$ a
$^{228}Th \rightarrow ^{224}Ra$	5.52	20.2	1.9116 a
$^{224}Ra \rightarrow ^{220}Rn$	5.79	21.7	3.6319 d
$^{220}Rn \rightarrow ^{216}Po$	6.40	25.0	55.6 s
$^{216}Po \rightarrow ^{212}Pb$	6.91	27.2	0.145 s
$^{212}Bi \rightarrow ^{208}Tl$	6.21*	23.9	60.55 min
$^{212}Po \rightarrow ^{208}Pb$	8.95	38.6	299 ns
^{238}U α-decay series			
$^{238}U \rightarrow ^{234}Th$	4.27	13.5	$4.468 \cdot 10^{9}$
$^{234}U \rightarrow ^{230}Th$	4.86	16.7	24.09 d
$^{230}Th \rightarrow ^{226}Ra$	4.77	16.2	75380 a
$^{226}Ra \rightarrow ^{222}Rn$	4.87	16.7	1600 a
$^{222}Rn \rightarrow ^{218}Po$	5.59	20.6	3.824 d
$^{218}Po \rightarrow ^{214}Pb$	6.12	23.4	3.10 min
$^{214}Po \rightarrow ^{210}Pb$	7.83	32.6	0.164 ms
$^{210}Po \rightarrow ^{206}Pb$	5.41	19.6	138.376 d

* 35.93% of decay

https://doi.org/10.1180/minmag.2013.077.6.12 Published online by Cambridge University Press

in equilibrium decay with the 0.3 at.% ^{238}U present, but the majority would have been derived from ^{232}Th, with a half-life of 1.4×10^{10} y, with the highest-energy α particles emitted at 8.95 MeV from ^{212}Po → ^{208}Pb decay (Gentry, 1974; Pal, 2004; NNDC, 2013; Table 1). As the monazite contains 0.3 at.% U, the U^{238} decay series will also have emitted α particles with an energy range of 4.3 to 7.8 MeV (Table 1). At 1.8 Ga, the original Th and U contents would have been 2.7 and 0.4 at.%, respectively.

On penetrating the biotite, the α-particles lose their energy and cause damage to the mineral structure by ionization, displacing atoms to produce interstitial atoms and vacancies as Frenkel pairs (FPs), and some thermal damage (Karsten and Ehrhart, 1995). Elastic collisions will cause displacements of 100s of atoms with most displacements taking place at the end of the particle's range as it loses energy. As a result of the different α-particles' energies in the decay series (Table 1), a point-source α-emitter should induce rings of 'damage' relating to the different penetration depths of the α particles. If the source mineral is greater than a few microns, then the rings are likely to be 'smeared' as the α particles could come from any part of the emitter and some will lose velocity before entering the biotite. Nasdala *et al*. (2001) calculated that the maximum vacancies created in biotite from a ^{238}U α-source would be at ~33 μm with the maximum ionization taking place at 31 μm from the emitter, although the penetration distances can be slightly modified by the Mg/Fe ratio of the host biotite. In the case of Th decay, five rings would potentially appear as there are overlaps in α-particle energy producing rings at ~20 μm (^{224}Ra and ^{228}Th) and ~24 μm (^{212}Bi and ^{220}Rn). Similarly, the energy of α-particles emitted by ^{234}U, ^{230}Th and ^{226}Ra decay are also very close as are those from ^{222}Rn and ^{210}Po, also suggesting five distinct rings (Gentry, 1974). The combination of the two decay series, emitters that are not point sources and long timescales should lead to a more pervasive sphere of damage.

Synchrotron investigation

Methods

The samples were analysed on the I18 beamline of the Diamond Light Source, UK (see Mosselmans *et al*., 2009). The experiments were performed using an approximately 3 μm beam focused by Kirkpatrick-Baez mirrors. Transmission diffraction images were recorded using an X-ray beam energy of 12 keV on a Photonic Science XDI-VHR 125 CCD over the range 12 to 44° 2θ. The diffraction set-up was calibrated using Si powder in the sample position. Typically acquisition times of 30 s per image were used. The images were analysed in *Igor Pro 6.1* (Wavemetrics Inc.) using the Nika plug-in

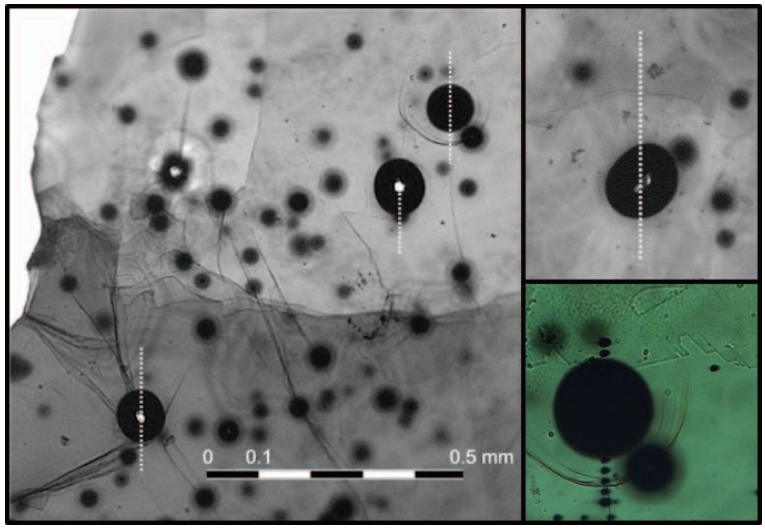

FIG. 2. Radiation damage haloes in biotite showing analytical traverses as white spots across the haloes. Several traverses were analysed.

https://doi.org/10.1180/minmag.2013.077.6.12 Published online by Cambridge University Press

(Ilavsky, 2012). The X-ray absorption spectra were collected in transmission mode using ion chambers filled with He. The beamline has a cryogenically cooled Si(111) monochromator. Harmonic rejection is achieved using the Kirkpatrick-Baez focusing mirrors which provide a cut-off around 18 keV. The spectra were calibrated against a spectrum of metallic Fe foil with the first inflection point set at 7111.2 eV. The XAS data was reduced in the program *Pyspline* (Tenderholt *et al*., 2007) and analysed in the program *DL-EXCURV* (Tomic *et al*., 2005). Both extended X-ray absorption fine structure (EXAFS) and X-ray absorption near-edge structure (XANES) data were collected at the Fe *K*-edge. The former yielded bond distances and coordination numbers for the Fe atoms in the biotite, and the latter provided information on the energy of the main absorption peak.

The samples were prepared as cleavage (*c*) parallel wafers mounted on a glass slide with a hole beneath selected areas of cleavage wafers 20 µm thick. Haloes were identified off-line on a high precision X−Y stage and transferred to the beamline. A sequence of points was chosen, at a minimum distance of 3 µm apart, in traverses from >100 µm outside the visible halo to the monazite inclusion. XAS analyses were conducted and followed by XRD analysis on the same spots. Several traverses across haloes were carried out and the results were reproducible (Fig. 2), with the focus of the study on the changes seen across the traverses.

X-ray absorption spectroscopy

Several traverses were analysed and representative EXAFS spectra from one traverse are presented in Fig. 3, with the full information extracted from the XAS traverse up to the monazite inclusion shown in Table 2 (spectra across the traverse are displayed in supplementary Figs S1 and S2, deposited with the Principal Editor at www.minersoc.org/pages/e_journals/dep_mat_mm.html). The Fe−Fe and Fe−O coordination numbers from Table 2 are plotted in Fig. 4*a* and *b* and show the Fe−Fe and Fe−O distances in unaffected biotite are 3.19(±0.1) Å and 2.085(±0.05) Å, respectively, taken from 20 points and typical of biotite (Brigatti *et al*., 2008). Only small variations are apparent across the traverse although there are differences between damaged and undamaged biotite (Fig. 4*a*,*b*). At the point the halo is encountered the Fe−Fe bond distance is at

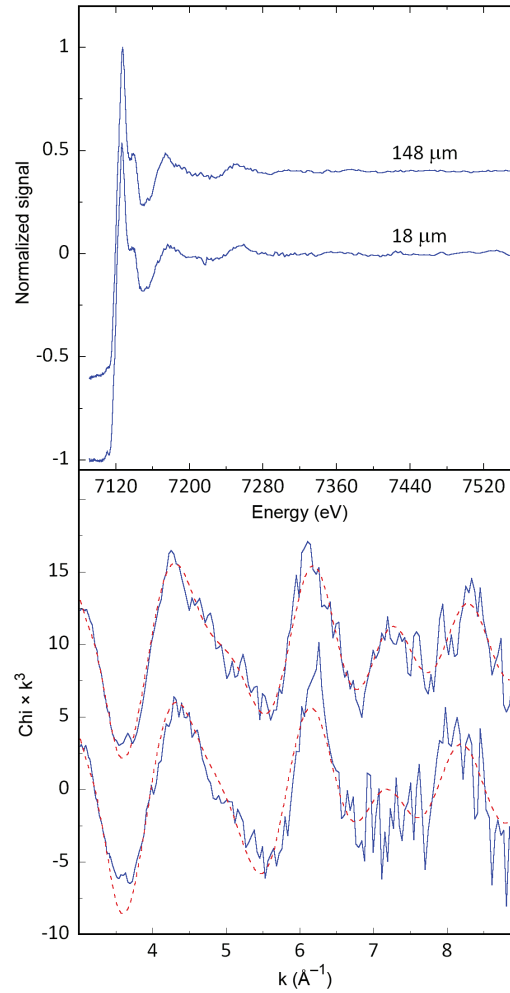

FIG. 3. *Upper*. Representative *K*-edge XAS spectra derived from a traverse across a damage halo, showing undamaged biotite 148 µm from the monazite and damaged biotite 18 µm from the monazite. *Lower*. The corresponding EXAFS (blue) and fits (dashed red) derived from them. (Structural data derived from the XAS are given in Table 2, and full spectra are shown in Figs S1 and 2.)

its lowest value of 3.16 Å, and the bond distances are more variable in the damage halo than the undamaged biotite (Fig. 4*a*). A pattern in the corresponding Fe−O distances is less clear but it shows small changes with the shortest Fe−O (2.07 Å) at the halo margin (diffuse zone) and the longest distances (2.10 Å) adjacent to the monazite. The most distinct changes between unaltered biotite and the damage halo are in the

https://doi.org/10.1180/minmag.2013.077.6.12 Published online by Cambridge University Press

TABLE 2. Fe *K*-edge EXAFS data derived from a traverse from undamaged biotite to the monazite inclusion.

Distance in μm from monazite	Scatterer	N	*r* (Å)	$2\sigma^2$ (Å^2)	R factor
148 undamaged	O	5.4	2.08	0.030	33.6
	Fe	4.4	3.19	0.025	
136	O	5.4	2.08	0.030	34.0
	Fe	4.3	3.18	0.028	
122	O	5.1	2.08	0.025	36.2
	Fe	5.0	3.20	0.030	
110	O	5.0	2.08	0.026	33.8
	Fe	3.9	3.19	0.027	
98	O	5.6	2.09	0.031	34.5
	Fe	3.9	3.20	0.023	
86	O	4.9	2.07	0.023	34.2
	Fe	4.2	3.20	0.024	
74	O	5.7	2.09	0.031	36.3
	Fe	5.4	3.19	0.030	
62	O	5.9	2.07	0.034	38.6
	Fe	5.7	3.18	0.034	
50	O	6.0	2.07	0.038	28.3
	Fe	4.6	3.18	0.028	
38	O	5.8	2.08	0.036	33.0
edge of halo	Fe	4.4	3.18	0.028	
33	O	5.3	2.06	0.034	32.5
	Fe	2.7	3.15	0.014	
28	O	5.4	2.09	0.037	33.8
	Fe	3.3	3.20	0.023	
23	O	4.9	2.09	0.032	38.2
	Fe	3.7	3.18	0.028	
18	O	4.5	2.08	0.018	43.9
	Fe	3.0	3.22	0.021	
13	O	5.0	2.08	0.028	53.1
	Fe	4.0	3.17	0.031	
8	O	5.1	2.10	0.034	44.9
	Fe	4.1	3.20	0.036	
3	O	5.8	2.10	0.039	54.4
	Fe	3.4	3.17	0.020	
0	O	5.0	2.09	0.033	48.3
Monazite	Fe	2.8	3.18	0.022	

Fe–Fe coordination numbers (N). In the unaltered biotite they are 4–6 (Fig. 4*b*, Table 2) and, as the Fe is in octahedral coordination, a value of 6 would be expected. It is worth noting that the N value from EXCURV can be lower than predicted, although relative comparisons are valid. Therefore the N values between 4 and 2.3 in the damage halo are significantly lower than those in the undamaged zone (Fig. 4*b*). XANES data (Fig. 5*a* and Fig. S1) were collected across several traverses and these displayed changes in the energy of the main Fe *K*-edge peak intensity which, though variable in clarity across different haloes, was consistent. The data show a change in this peak position from 7131.5 eV in the unaltered biotite to between 0.5 to 1.0 eV lower in the halo. In two cases, just before the visible dark halo was reached, the peak position increased in energy by 0.4 eV (Fig. 5*a* and *b*). The shift of Fe *K*-edge XANES 'peak' to lower energies within the damaged halo indicates a lowering of the average binding energy for the iron and therefore a reduction of the Fe^{3+} component in the biotite by the α-particle bombardment (Waychunas *et al.*, 1983; Berry *et al.*, 2013). Mössbauer analysis indicates that 10 at.% of the iron in undamaged

https://doi.org/10.1180/minmag.2013.077.6.12 Published online by Cambridge University Press

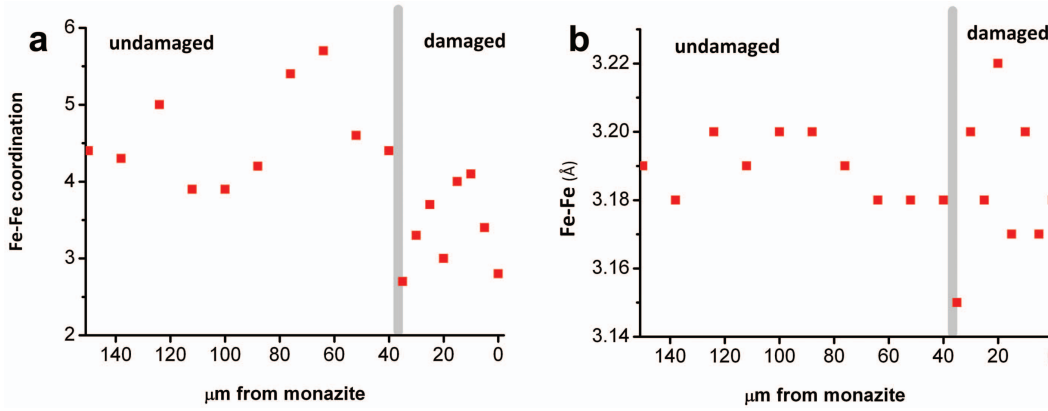

FIG. 4. Plots showing structural parameters determined by EXAFS from the representative traverse across a radiation-damaged halo in biotite (Table 2): (*a*) the Fe–Fe bond distances, (*b*) Fe co-ordination number (N).

biotite is Fe^{3+}, therefore the 0.5–1.0 eV shift in peak position suggests a significant proportion of the Fe^{3+} in the biotite has been reduced.

The XAS reveals evidence of both a loss in local atomic ordering and Fe-reduction in the damage halo. The data are also erratic, showing that in the sampled volume (beam size 9 μm^2, with a sample thickness of ~20 μm) there are localized variations in the amount of damage induced by the α-bombardment.

The reduction of the Fe by α-particles ($^4_2He^{2+}$), can be explained by electronic collisions that produce a track of electronic holes and a cascade of secondary electrons with energies up to 100 eV. As the electrons travel away from the primary source, energy transfer events mean they gradually lose energy before localizing and becoming trapped. Low- and thermal-energy electrons are highly reducing and will easily reduce Fe^{3+}centres to Fe^{2+},

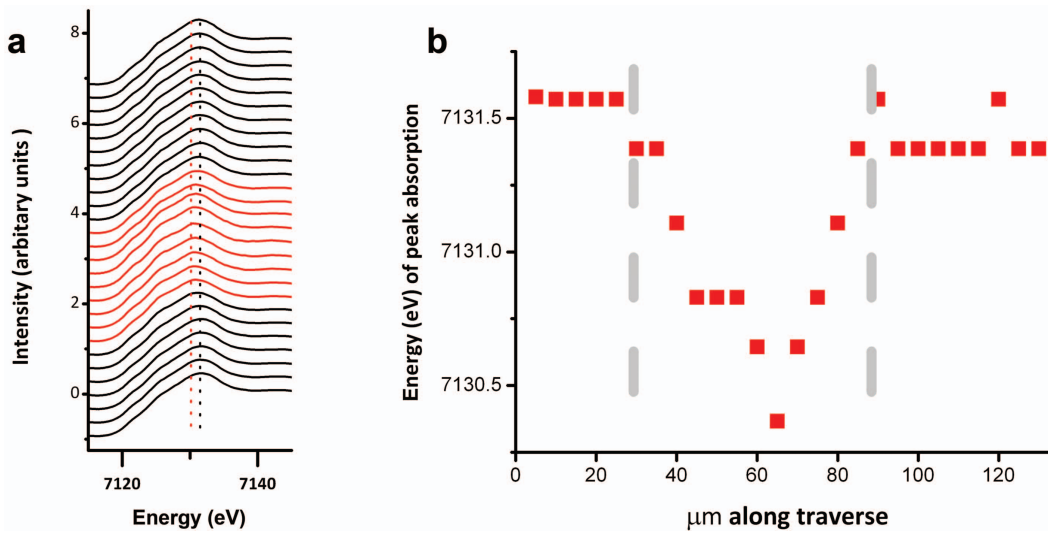

FIG. 5. (*a*) Fe *K*-edge XANES spectra traverse across a complete visible radiation-damage halo in biotite around a 3 μm monazite inclusion; the spectra in red are from the damage zone. (*b*) Plot of the maximum absorption energies in the Fe *K*-edge XANES traverse across the visible radiation-damage halo in biotite in (halo between vertical dashed lines).

https://doi.org/10.1180/minmag.2013.077.6.12 Published online by Cambridge University Press

becoming trapped at that location. In biotite the Fe is in edge sharing, octahedral coordination in the trioctahedral sheets, occupying two distinct sites, with the Fe^{3+} preferentially residing in the '*M*2' sites and Fe^{2+} in the other, larger, '*M*1' sites. Both sites are bonded to OH-groups, with *M*1 sites the OH in opposite, *trans* positions and the *M*2 in adjacent *cis* positions (see Cruciani and Zanazzi, 1994; Virgo and Popp, 2000; Mesto *et al*., 2006; Brigatti and Guggenheim, 2002; Manova *et al*., 2009). The reduction of the Fe^{3+} by the α-particles, with the biotite lattice acting as an electron acceptor, may not be by direct electron transfer. One possible mechanism is via the radiolysis of the OH groups present producing hydrogen for loca-

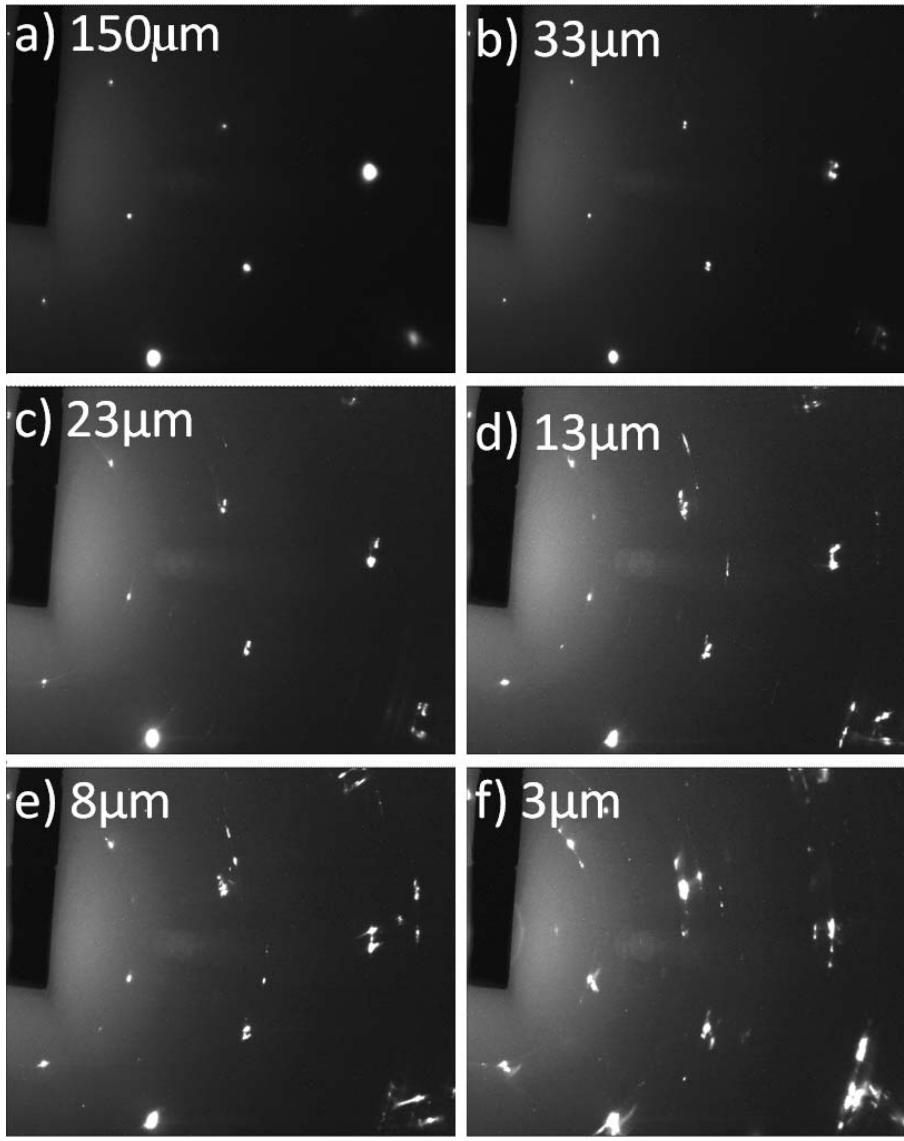

FIG. 6. (*a*–*f*) Selected transmission diffraction patterns from a traverse across a visible damage halo in biotite showing increasing structural damage as the monazite crystal is approached. Beam size was 3 µm; distances relate to the centre of the beam in relation to the edge of the monazite.

https://doi.org/10.1180/minmag.2013.077.6.12 Published online by Cambridge University Press

lized Fe^{3+} reduction ($Fe^{3+} + H^0 \rightarrow Fe^{2+} + H^+$) and evidence for the role of OH in this process is supported by the loss of the definition of the OH in the Raman spectra in the damaged halo areas of biotite, seen in previous studies (Vance, 1978; Seal *et al*., 1981). Rosso and Ilton (2005) have also demonstrated a mechanism of Fe^{II}/Fe^{III} electron transfer in biotite across edge-sharing octahedral *M*2–*M*2 sites, facilitating electron transfer and reduction; this process would also be assisted by the large number of unoccupied octahedral sites (up to 20%) in Fe-rich biotites (Manova *et al*., 2009). In their study, Nasdala *et al*. (2001) interpret the loss of intensity of the OH-band as being related to charge imbalances around the H atoms caused by displacive or ionising events. However, they noted that the lack of changes in optical absorbance spectra, especially the Fe^{2+}/Fe^{3+} absorption bands, indicated ionization effects were not important. The greater Fe content of the biotite in this study and the much higher α-particle flux compared to their 'emitter' zircons may explain this difference. If any Fe^{3+} is present in the tetrahedral sites in biotite it is unlikely to be reduced as the increase in ionic radii of Fe^{2+} precludes its incorporation.

X-ray diffraction

The XRD pattern in the traverse across the undamaged biotite displays distinct biotite reflections but as the monazite inclusion is approached, these reflections become fragmented and relatively diffuse. Six points ([a]–[f]) across the traverse are used to illustrate these changes which are shown in Figs 6 and 7 with a summary of the *d* spacing and intensity data presented in Table 3. The quality of the diffraction data means the appearance/disappearance of small peaks must be interpreted with caution and the accuracy of *d* spacing values is probably ±0.1 Å. As the X-ray beam was perpendicular to the basal *c* axis of the biotite, the {001} reflections are minimized, and reflections in the *a*–*b* plane enhanced. In any case the highest intensity 001 reflection, with a *d* spacing of ~10.1 Å, is outside the range of the geometry of the experiment and the 002 and 007 reflections are seen as very small intensities and the $13\bar{1}$ biotite reflection is not seen. In comparison with the standard PXRD of the biotite (not shown) the same intensities are observed in the synchrotron XRD except for the 110 reflection, which is poorly developed in conventional PXRD, but clearly seen in Figs 6 and 7.

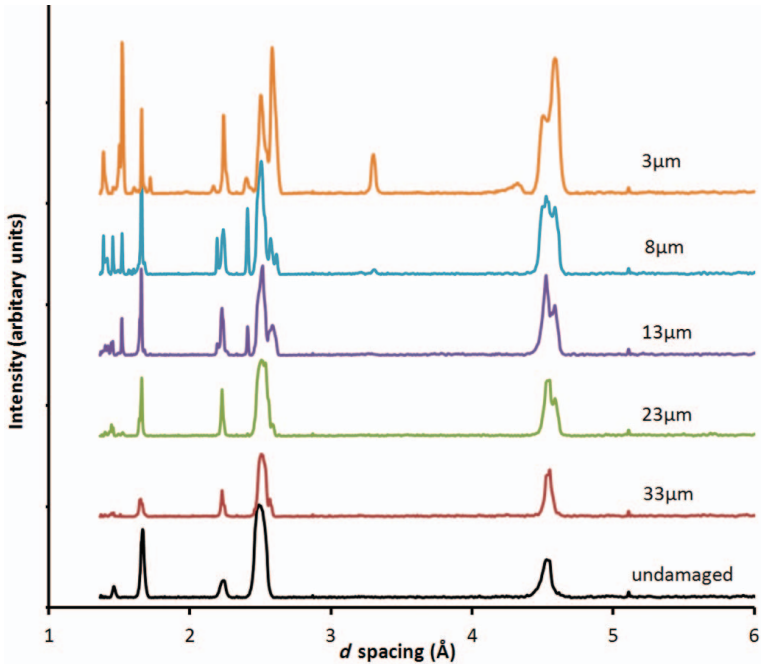

FIG. 7. Diffraction patterns derived from Fig. 6, showing the splitting of peaks and intensity variations as the monazite is approached (see text and Table 3 for quantification of the peak positions and intensities).

https://doi.org/10.1180/minmag.2013.077.6.12 Published online by Cambridge University Press

TABLE 3. *d* spacings, in Å, derived from the selected synchrotron diffraction points, [a]-[f] Figure 6. *d* = *d* spacing; I = intensity (% highest). *hkl* derived from comparison with published data (Fletcher *et al*., 1996) and PXRD analysis of the biotite used in this study.

hkl	[a] *d*	[a] I	[b] *d*	[b] I	[c] *d*	[c] I	[d] *d*	[d] I	[e] *d*	[e] I	[f] *d*	[f] I
Unalloc.									1.39	20	1.39	20
					1.40	2	1.40	5	1.40	10		
							1.41	5	1.41	10	1.41	10
					1.43	4						
					1.44	4	1.44	8				
007	1.46	15	1.46	5	1.45	7	1.45	10	1.45	30	1.45	5
$\bar{3}31$					1.49	2					1.51	20
					1.53	5	1.52	35	1.52	40	1.52	80
Unalloc.									1.56	3		
									1.57	3		
											1.61	5
									1.59	3		
204					1.64	33			1.64	7		
					1.65	55	1.65	30				
$\bar{1}35$	1.66	70	1.65	25	1.66	20			1.66	80	1.66	70
									1.67	10		
Unalloc.											1.72	10
Unalloc.											2.16	50
							2.19	7	2.19	25		
202	2.23		2.23	30	2.23	60	2.23	35			2.23	50
	to						2.24	20	2.24	30		
$\bar{1}33$	2.25	20	2.25	15	2.25	10						
											2.26	7
201					2.41	5	2.41	25	2.41	65	2.40	15
$\bar{1}32$							2.48	70	2.48	70		
	2.49	100										
											2.50	75
			2.51	100	2.50	90	2.51	100	2.51	100		
					2.53	100						
											2.54	40
					2.56	15	2.56	30				
									2.57	25		

https://doi.org/10.1180/minmag.2013.077.6.12 Published online by Cambridge University Press

200			2.58	20	2.58	8	2.58	30			2.58	100
									2.61	15		
13$\bar{1}$					2.63	5						
Monazite									3.35	4	3.35	25
110									4.50	70	4.50	60
	4.52	60	4.52	80	4.52	90	4.52	90	4.52	75		
									4.53	70		
			4.55	80	4.55	90						
							4.56	50				
					4.59	60	4.59	60	4.59	70	4.59	90
											4.61	50
002	5.11	5	5.11	5	5.11	5	5.11	5	5.11	5	5.11	5
hkl	[a] D	[a] I	[b] d	[b] I	[c] d	[c] I	[d] D	[d] I	[e] d	[e] I	[f] d	[f] I

Reflections in the range d = 4.50–4.61, the 110 reflection. The biotite 110 reflection produces a single entity at d = 4.52 Å in [a] (Fig. 6). As the monazite is approached, one intensity with lower d (4.50 Å) and one with higher d (4.59 Å) develop steadily, the latter becoming the dominant reflection in [f]. In addition, the reflection at d = 4.52 Å is split in [e] and the peak at d = 4.59 Å splits in [f] with a further resolvable reflection at d = 4.61 Å.
Reflections, 13$\bar{2}$, in the range d = 2.48 to 2.58 Å. The high-intensity reflection seen with a peak at 2.49 Å in [a] has a larger d spacing of 2.51 Å in [b] where new reflections appear at larger values of d. In [c] there is a peak at d = 2.53 Å and a high-intensity peak at ~2.51 Å. In [d] and [e] this latter reflection appears to become more distinct and move to slightly lower d values with the reflections ~2.56 Å developing.
The peak at d = 2.58 Å in [b] is a major intensity in [f], coincident with the expected value for 200 although this is not seen in the undamaged biotite.
Peaks with d = 2.23/2.25 Å are likely to be a combination of 202 and $\bar{1}$33 and there is clearer evidence of two resolvable reflections in [b] which persist as the emitter is approached, both showing a minor reduction in d.
Reflections in the range d = 1.64–1.69 Å. The expected reflections at this value of d are 204 and $\bar{1}$35. A decrease in d value, is seen. The apparent split in [c] may be better resolution of these reflections, or a genuine splitting of intensities of one of the reflections. Small, new reflections are seen in the range d = 1.59–1.67 Å in [e,f].
Unallocated reflections at d = 1.53 Å increase rapidly as the emitter is approached, a new reflection develops at d = 1.51 Å.
A small reflection at d = 1.45 Å (007 reflection) is seen in the unaffected biotite. Several small reflections develop between d = 1.43 and 1.39 Å, especially in [c], where there is the first appearance of an intensity at d = 1.40 Å which 'splits' and intensifies as the emitter is approached.
The reflection at 3.35 Å is coincident with the 100 intensity expected in monazite.

https://doi.org/10.1180/minmag.2013.077.6.12 Published online by Cambridge University Press

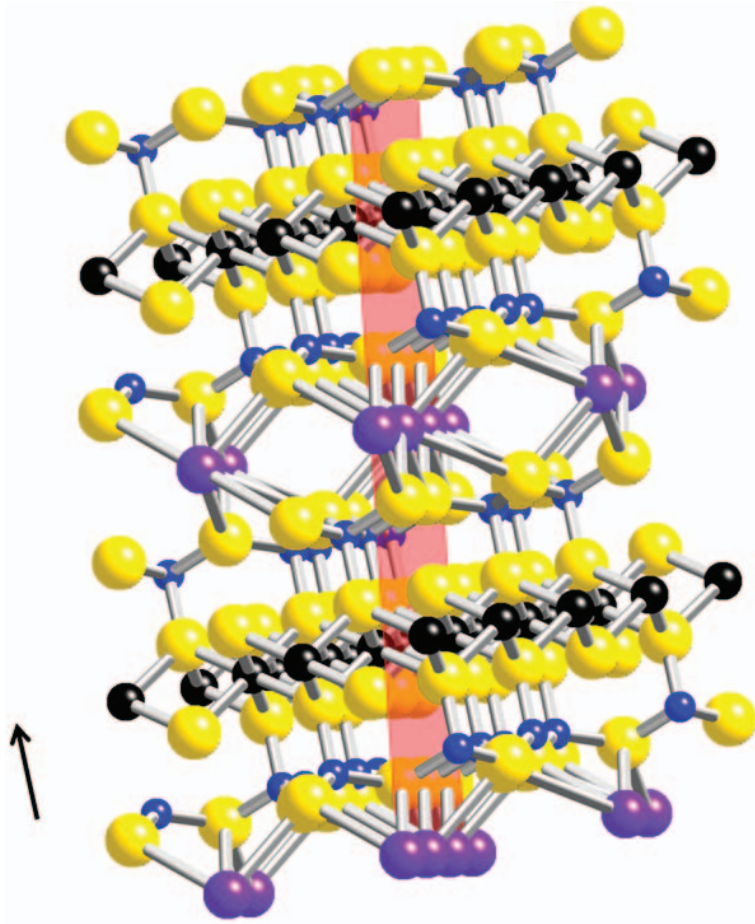

FIG. 8. Representation of the biotite atomic structure showing the trioctahedral layers containing transition-metal cations ($Fe^{2+}Fe^{3+}$, Ti, Mg, Mn = black) between two tetrahedral Si layers (Si/Al = blue); O atoms are yellow. The layers are joined by the interlayer cations, K and/or Na (purple). These layers form the *a*,*b* layers in biotite, which were oriented at right angles to the synchrotron beam which was parallel to *c* (arrowed). (110) is shown (pink). (model derived from Crystalmaker ®)

Despite the uncertainties in assigning reflections, extensive structural changes in the biotite diffraction are observed. Of the major biotite reflections observed in the synchrotron data, the 110 (see Fig. 8) records development of a new structural component with a larger *d* spacing than undamaged biotite, and several new 'domains' emerge as the α-emitter is approached. Some of these new reflections also record a decrease in *d*. The suite of reflections in the range *d* = 2.48–2.58 Å ($\bar{1}32$ reflections) reveal similar changes in the structure, with a component of the biotite apparently remaining 'undamaged' with 'satellites' representing regions of larger and smaller *d* spacing developing. A more consistent drop in *d* value as the monazite is approached is seen for the *d* = 1.64–1.67 Å 204/$\bar{1}35$ reflections.

These new reflections and the emergence of rings in the diffraction pattern (Fig. 6) reveal the development of polycrystallinity in the damaged biotite and the growth of domains of a new ordered structure in which the cell *a*,*b* parameters have been changed. In α-particle bombardment the defects occur by displacement of the cations and the formation of interstitial cations which would result in an increase in cell parameter. It is noted that there are small reflections at *d* = 1.39 Å, 1.41 Å, 1.51 Å, 1.61 Å, 1.72 Å, 1.53 Å,

https://doi.org/10.1180/minmag.2013.077.6.12 Published online by Cambridge University Press

2.19 Å and 2.41 Å which are difficult to assign and did not appear in the undamaged biotite, the most intense of these are the reflections at d = 2.19 Å and 1.51 Å. They could represent changes in diffraction conditions after damage but it is not possible to assign them with confidence to biotite reflections. One possibility is that they represent development of new phases with damage; goethite, magnetite, wüstite, chlorite, orthopyroxene all develop from alteration and metamorphic (dehydration) reactions of biotites but there is no other evidence to support this. To resolve some of the uncertainties in the diffraction, dedicated, high-resolution micro-diffraction is required.

Discussion

The XAS data show the damaged biotite has a disrupted short-range order (as represented by the iron coordination) and the Fe^{3+} is reduced, while the XRD data reveal the damaged biotite is a polycrystalline mosaic of structural domains, with both smaller but mainly larger d spacings than the undamaged biotite. As an α particle penetrates an insulating material like biotite it is attenuated by collisions with the electrons and atomic nuclei of the material. The α particles passing through the biotite will have initially lost energy in small amounts due to interactions with the electrons surrounding the biotite atoms (Coulombic interactions). Electronic collisions result predominantly in ionization. Nuclear collisions between an α particle and atomic nuclei are primarily responsible for displacement of the nuclei and are found only at the very end of the α particles' trajectory, when the particle energy drops below that needed to excite the electrons. These collisions occur along the length of an α particle's trajectory, although the density increases as the energy of the ion decreases. Figure 9*a* shows the electronic stopping power and range of biotite as a function of α particle penetration for ions with initial energy 4, 7 and 8 MeV (see also Table 1), calculated using *SRIM-2008.04* code (Zeigler, 2011). This figure shows the change in α particle stopping power along a single ion track. The higher-energy particles are calculated to penetrate further than those presented in Table 1, but at lower energies the values are similar. In the results presented here the first real evidence of damage in the halo (show in Fig. 6*c*) is at ~25 µm from the emitter, coincident with the end of the penetration range of several of the ^{232}Th decay series where the nuclei collisions are likely. However, to fully understand electronic damage around a ^{238}U/^{232}Th-containing inclusion, it is necessary to consider the density of electronic energy transferred as a function of distance from the inclusion. The electronic stopping flux of biotite (see chemical formula above) is expressed as a function of ion penetration for $^{4}_{2}He^{2+}$ ions of energy 4, 7 and 8 MeV and is shown in Fig. 9*b*. Electronic stopping flux has been arbitrarily defined as the electronic stopping power divided by the square of the ion range and is a measure of

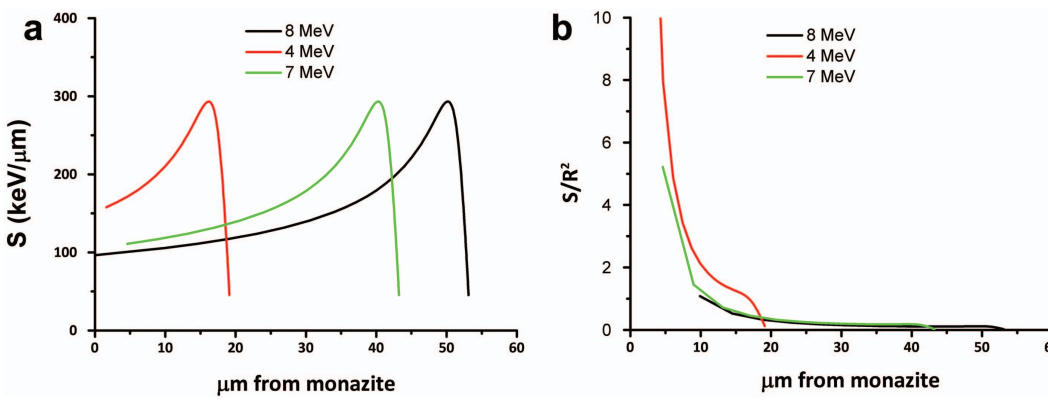

FIG. 9. (*a*) Electronic stopping power of biotite, $K_{0.94}Na_{0.03}Fe_{1.95}Mg_{0.91}Mn_{0.05}Ti_{0.02}Al_{1.25}Si_{2.84}O_{10}(OH)_2$, expressed as a function of ion penetration for $^{4}_{2}He^{2+}$ ions of energy 4 (red), 7 (green) and 8 (black) MeV calculated using *SRIM-2008.04* (Zeigler, 2011). (*b*) Electronic stopping flux of biotite, $K_{0.94}Na_{0.03}Fe_{1.95}Mg_{0.91}Mn_{0.05}Ti_{0.02}Al_{1.25}Si_{2.84}O_{10}(OH)_2$, expressed as a function of ion penetration for $^{4}_{2}He^{2+}$ ions of energy 4 (red), 7 (green) and 8 (black) MeV calculated using *SRIM-2008.04* (Zeigler, 2011).

https://doi.org/10.1180/minmag.2013.077.6.12 Published online by Cambridge University Press

the density of energy deposition. Strictly, the density of energy deposition is the electronic stopping flux divided by 4π. From Fig. 9*b* it is clear that the vast majority of electronic energy loss by the α particle emitted from the inclusion will occur within 8 mm of the inclusion irrespective of the α energy. Thus, although the development of rings of damage clearly occurs in biotites, in these samples the large amount of damage observed close to the monazite is better explained by an electron stopping flux model. As the α-particle interactions with the biotite lattice will be most intense where there are large electron densities, these will be focused on the trioctahedral layers, including the Fe, (Fig. 8), with little impact on the interlayers occupied by K/Na atoms.

The main mechanism of local lattice distortion in the biotites studied here would have been by development of defects (Frenkel pairs) which can persist for over 1.0 Ga (Ewing, 1994; Weber *et al*., 1994). Typically Frenkel pairs would lead to diffuse scattering around the 'undamaged' biotite reflections, and the interstitial atoms would contribute to the larger *d*-spacing component. If the defect density reaches a critical value, amorphization occurs and there is an attendent volume increase (Holland and Gottfried 1955; Redfern 1996; Motta, 1997; Ewing, 2000; Ewing *et al*., 2003). However, the diffraction data presented here give evidence of new domains of ordered structure with relatively sharp diffraction peaks, and only a little evidence of diffuse scattering and no evidence of extensive amorphization. The development of domains can be enhanced by the preferential destruction of specific sites such as the OH groups (dehydration) by local protonation and thermal effects; this would also lead to cell-size increases (see Nasdala *et al*., 2001; Miro *et al*., 2004). Although there may be radiolytic disruption of OH bonds, the SiO_4 units (Fig. 8) generally hold together (Wang *et al*., 1991; Weber *et al*., 1994).

The diffraction data show both increases and decreases in *d* spacings, as well as domains of unaffected structure. This irregularity in the distribution of damage may be similar to the 'islands' of undamaged structure seen in severely damaged actinide-bearing minerals (Ewing, 2000) where recoil was the main damage mechanism. (110) comprises silica tetrahedra joining the trioctahedral layers (Fig. 8) and the change in *d* spacing in the damaged zones reveals expansion of biotite in the distances between the trioctahedral layers. Displacement of the metal ions and loss of OH groups would be consistent with this change; re-crystallization by gliding parallel to the (110) crystallographic plane would facilitate the development of crystalline sub-domains. In contrast, the 204 reflection provides evidence of a *d* spacing decrease and this might reflect shrinkage of the trioctahedral layer, explainable if the interstitial atoms are displaced out of this plane (Fig. 8).

Acknowledgements

The authors are grateful to the STFC and Diamond Light Source for access to the Synchrotron under access SP585. We thank Tim Hopkins for assistance with the EPMA and Harri Williams for help preparing samples. Simon Redfern is thanked for constructive comments.

References

Berry, A.J., Yaxley, G.M., Hanger, B.J., Woodland A.J., de Jonge, M.D., Howard, D.L., Paterson, D. and Kamenetsky, V.S. (2013) Quantitative mapping of the oxidative effects of mantle metasomatism. *Geology*, doi:10.1130/G34119.1

Brigatti, M.F. and Guggenheim, S. (2002) Mica crystal chemistry and the influence of pressure, temperature, and solid solution on atomistic models. Pp. 1–97 in: *Micas: Crystal Chemistry and Metamorphic Petrology* (A. Mottana, F.P. Sassi, J.B. Thompson Jr. and S. Guggenheim, editors). Reviews in Mineralogy and Geochemistry, **46**, Mineralogical Society of America and The Geochemical Society, Chantilly, Virginia, USA.

Brigatti, M.F., Guidotti, C.V., Malferrari, D. and Sassi, F.P. (2008) Single-crystal X-ray studies of trioctahedral micas coexisting with dioctahedral micas in metamorphic sequences from western Maine. *American Mineralogist*, **93**, 396–408.

Cruciani, G. and Zanazzi, P.F. (1994) Cation partitioning and substitution mechanisms in 1M-phlogopite: a crystal chemical study. *American Mineralogist*, **78**, 289–301.

Ewing, R.C. (2000) Radiation-induced amorphization. Pp. 319–361 in: *Transformation Processes in Minerals* (S.A.T. Redfern and M.A. Carpenter, editors). Reviews in Mineralogy and Geochemistry, **39**. Mineralogical Society of America and The Geochemical Society, Chantilly, Virginia, USA.

Ewing R.C. (2001) The design and evaluation of nuclear waste forms: Clues from mineralogy. *The Canadian Mineralogist*, **39**, 697–715.

Ewing, R.C. (1994) The metamict state: 1993 – The

https://doi.org/10.1180/minmag.2013.077.6.12 Published online by Cambridge University Press

Centennial. *Nuclear Instruments and Methods in Physics Research*, **B91**, 22–29.

Ewing, R.C., Meldrum, A., Wang, L., Weber, J. and Corrales, R. (2003) Radiation effects in zircon. Pp. 387–426 in: *Zircon* (J.M. Hanchar and P.W.O. Hoskins, editors). Reviews in Mineralogy and Geochemistry, **53**. Mineralogical Society of America and The Geochemical Society, Chantilly, Virginia, USA.

Fleet, M.E. (2003) *Rock-Forming Minerals, Volume 3A Sheet Silicates: Micas*. The Geological Society, London. 758 pp.

Fletcher, D.A., McMeeking, R.F. and Parkin, D. (1996) The United Kingdom Chemical Database Service. *Journal of Chemical Information and Computer Science*, **36**, 746–749.

Gentry, R.V. (1974) Radiohaloes in a radiochronological and cosmological perspective. *Science*, **184**, 62–66.

Henry, N.F.M. (1935) Some data on the iron-rich hypersthenes. *Mineralogical Magazine*, **24**, 221–226.

Holland, H.D. and Gottfried D. (1955) The effect of nuclear radiation on the structure of zircon. *Acta Crystallographica*, **8**, 291–300.

Ilavsky, J. (2012) Nika: software for two-dimensional data reduction. *Journal of Applied Crystallography*, **45**, 324–328.

Joly, J. (1917) The genesis of pleochroic halos. *Philosophical Transactions of the Royal Society of London*, Series A, **217**, 51.

Karsten, K. and Ehrhart, P. (1995) Frenkel pairs in low-temperature electron irradiated InP: X-ray diffraction *Physics Review*, **B51**, 10508–10519.

Manova, L.J., Connolly, J.A.D. and Cesare, B. (2009) A thermodynamic model for titanium and ferric iron solution in biotite. *Journal of Metamorphic Geology*, **27**, 153–165.

Mesto, E., Schingaro, E., Scordari, F. and Ottolini, L. (2006) An electron microprobe analysis, secondary ion mass spectrometry, and single-crystal X-ray diffraction study of phlogopites from Mt. Vulture, Potenza, Italy: Consideration of cation partitioning. *American Mineralogist*, **91**, 182–190.

Miro, S., Grebille, D., Chateigner, D., Pelloquin, D., Stoquert, J.P., Grob J.-J., Costantini, J.M. and Studer, F. (2004) Changes in X-ray diffraction study of damage induced by swift heavy ion irradiation in fluorapatite. *Nuclear Instruments and Methods in Physics Research*, **B 227**, 306–318.

Mosselmans, J.F.W., Quinn, P.D., Dent, A.J., Cavill, S.A., Diaz Moreno, S., Peach, A., Leicester, P.J., Keylock, S.J., Gregory, S.R., Atkinson, K.D. and Roque Rosell, J. (2009) I18 – the microfocus spectroscopy beamline at the Diamond Light Source. *Journal of Synchrotron Radiation*, **16**, 818–824.

Motta, A.T. (1997) Amorphization of intermetallic compounds under irradiation: a Review. *Journal of Nuclear Materials*, **244**, 227–250.

Murakami, T., Chakoumakos, B.C., Ewing, R.C., Lumpkin, G.R. and Weber, W.J. (1991) Alpha-decay damage in zircon. *American Mineralogist*, **76**, 1510–1532.

Nasdala, L., Wenzel, M., Andrut, M., Wirth, R. and Blaum, P. (2001) The nature of radiohaloes in biotite: experimental studies and modeling. *American Mineralogist*, **86**, 498–512.

Nasdala, L., Hanchar, J.M, Kronzc, A. and Whitehouse, M.J. (2005) Long-term stability of alpha particle damage in natural zircon. *Chemical Geology*, **220**, 83–103.

National Nuclear Data Center (2013) Brookhaven Nuclear Science References. Chart of Nuclides version of 2013. (Information extracted from the NSR database based on ENSDF and Nuclear Data Sheets).

Pal, D.C. (2004) Concentric rings of radioactive halo in chlorite, Turamdih uranium deposit, Singhbhum Shear Zone, Eastern India: a possible result of ^{238}U chain decay, *Current Science*, **87**, 662–667.

Palmgren, J. (1917). The eulysite of Södermanland. *Bulletin of the Geological Institute of the University of Uppsala*, **14**, 109–228.

Pouchou, J.L. and Pichoir, F. (1991) Quantitative analysis of homogeneous or stratified microvolumes applying the model "PAP". Pp. 31–75 in: *Electron Probe Quantitation* (K.F.J. Heinrich and D.E. Newbury, editors). Plenum Press, New York.

Redfern, S.A.T. (1996) Length scale dependence of high-pressure amorphization: static amorphization of anorthite. *Mineralogical Magazine*, **60**, 493–498.

Rosso, K.M. and Ilton, E.S. (2005) Effects of compositional defects on small polaron hopping in micas. *Journal of Chemical Physics*, **122**, 244709.

Seal, M., Vance, E.R. and Demayo, B. (1981) Optical spectra of giant radiohaloes in Madagascan biotite. *American Mineralogist*, **66**, 358–361.

Sundius, N. (1932) Über den sogennanten Eisenanthophyllit der Eulysite. *Årsbok, Sveriges Geologiske Undersökning*, **26**, 6–118.

Tenderholt, A., Hedman, B. and Hodgson, K.O. (2007) PySpline: A modern, cross-platform program for the processing of raw averaged XAS edge and EXAFS data. *American Institute of Physics Conference Proceedings*, **882**, 105–107. 13th International Conference on X-ray Absorption Fine Structure XAFS13.

Tomic, S., Searle, B.G., Wander, A., Harrison, N.M., Dent, A.J., Mosselmans, J.F.W. and Inglesfield, J.E. (2005) New Tools for the Analysis of EXAFS: The DL EXCURV Package. *CCLRC Technical Report DL-TR-2005-001*, ISSN 1362-0207.

https://doi.org/10.1180/minmag.2013.077.6.12 Published online by Cambridge University Press

Vance, E.R. (1978) Possible mechanism for the formation of bleached, giant haloes in Madagascan mica. Pp. 228–235 in: *Superheavy Elements: Proceedings of the International Symposium on Superheavy Elements, Lubbock, March 9–11, 1978* (M.A.K. Lodhi, editor). Pergamon, UK.

Virgo, D. and Popp, R.K. (2000) Hydrogen deficiency in mantle-derived phlogopites. *American Mineralogist*, **85**, 753–759.

Wang, L.M., Eby, R.K., Janeczek, J. and Ewing, R.C. (1991) *In situ* TEM study of ion-beam-induced amorphization of complex silicate structures. *Nuclear Instruments and Methods for Physics Research*, **B59/60**, 395–400.

Waychunas, G.A., Apted, M.J. and Brown G.E., Jnr. (1983) X-ray K-edge absorption spectra of Fe minerals and model compounds: Near-edge structure. *Physics and Chemistry of Minerals*, **10**, 1–9.

Weber, W.J., Ewing, R.C. and Wang, L.M. (1994) The radiation-induced crystalline-to-amorphous transition in zircon. *Journal of Materials Research*, **9**, 688–698.

Ziegler, J.F. (2011) //SRIM: the Stopping and Range of Ions in Matter (www.srim.org).

Zhao, G.C., Cawood, P.A., Wilde, S.A. and Sun, M. (2002) Review of global 2.1–1.8 Ga orogens: implications for a pre-Rodinia supercontinent. *Earth Science Reviews*, **59**, 125–162.

https://doi.org/10.1180/minmag.2013.077.6.12 Published online by Cambridge University Press